

A study of the radio spectrum of Mrk 421

JEE WON LEE,¹ SANG-SUNG LEE,^{1,2} JEFFREY HODGSON,³ ALGABA JUAN-CARLOS,⁴ SANG-HYUN KIM,^{1,2}
WHEE YEON CHEONG,^{1,2} HYEON-WOO JEONG,^{1,2} AND SINCHEOL KANG¹

¹*Korea Astronomy and Space Science Institute, 776 Daedeok-daero, Yuseong-gu, Daejeon 34055, Republic of Korea*

²*University of Science and Technology, 217 Gajeong-ro, Yuseong-gu, Daejeon 34113, Korea*

³*Department of Physics and Astronomy, Sejong University, 209 Neungdong-ro, Gwangjin-gu, Seoul, South Korea*

⁴*Department of Physics, Faculty of Science, Universiti Malaya, 50603 Kuala Lumpur, Malaysia*

Submitted to ApJ

ABSTRACT

We present the results of a spectral analysis using simultaneous multifrequency (22, 43, 86, and 129 GHz) very long baseline interferometry (VLBI) observations of the Korean VLBI Network (KVN) on BL Lac object, Markarian 421 (Mrk 421). The data we used was obtained from January 2013 to June 2018. The light curves showed several flux enhancements with global decreases. To separate the variable and quiescent components in the multifrequency light curves for milliarsecond-scale emission regions, we assumed that the quiescent radiation comes from the emission regions radiating constant optically-thin synchrotron emissions (i.e., a minimum flux density with an optically thin spectral index). The quiescent spectrum determined from the multifrequency light curves was subtracted from the total CLEAN flux density, yielding a variable component in the flux that produces the time-dependent spectrum. We found that the observed spectra were flat at 22-43 GHz, and relatively steep at 43-86 GHz, whereas the quiescent-corrected spectra are sometimes quite different from the observed spectra (e.g., sometimes inverted at 22-43 GHz). The quiescent-corrected spectral indices were much more variable than the observed spectral indices. This spectral investigation implies that the quiescent-spectrum correction can significantly affect the multifrequency spectral index of variable compact radio sources such as blazars. Therefore, the synchrotron self-absorption B-field strength (B_{SSA}) can be significantly affected because B_{SSA} is proportional to the fifth power of turnover frequency.

Keywords: BL Lacertae objects: individual (Mrk 421)—galaxies:active — quasars: relativistic jets—radio continuum: galaxies

1. INTRODUCTION

Active Galactic Nuclei (AGN) are the central regions of galaxies that exhibit unusually bright luminosity across multiwavelengths, from radio to gamma rays. It is thought that the mechanism responsible for this luminosity is a supermassive black hole ($10^6 - 10^{10} M_{\odot}$) at the center of the AGN, which accretes enormous amounts of matter from its surrounding environment. A relativistic jet is formed by the accreted matter (Ulrich et al. 1997).

A blazar is a subclass of AGN that exhibits extremely energetic and highly variable observational behavior. The source is among the most luminous and powerful objects, and features a relativistic jet that points directly toward us with a very small viewing angle. This alignment causes a blazar to appear as a point-like source in the sky that exhibits rapid and dramatic variability in its brightness (Urry & Padovani 1995). Blazars encompass both BL Lac objects and flat-spectrum radio quasars (FSRQs). While FSRQs and BL Lac objects share similar characteristics, such as being highly variable and bright, their spectra differ. The spectrum of a BL Lac object has weak or no broad emission, unlike that of an FSRQ.

Markarian 421 (Mrk 421), is one of the most extensively studied high-synchrotron-peaked blazars and one of the closest sources, located at a redshift $z=0.031$. Its high luminosity enables us to investigate its emission (Katarzyński et al. 2003; Charlot et al. 2006; Horan et al. 2009; Acciari et al. 2011; Aleksić et al. 2015; Arbet-Engels et al. 2021). Its source Mrk 421 was the first extragalactic source detected in the TeV energy bands, as reported by Punch et al. (1992) using the Whipple 10-m Cherenkov telescope. Mrk 421 is classified as a BL Lac object.

Acciari et al. (2011) reported no correlation between TeV γ -ray and optical/radio light curves obtained from observations performed from December 2005 to May 2008 with VERITAS/Whipple gamma-ray data and Metsahovi and UMRAO radio data. On the other hand, when focusing on the very high energy (VHE) $E > 100$ GeV, they found a strong correlation between TeV gamma-ray and X-rays and suggested that this can be explained by the one-zone synchrotron self-Compton model (Zhu et al. 2016). In a multiwavelength study conducted on Mrk 421 over 5.5-yr period, from December 2012 to April 2018, Arbet-Engels et al. (2021) performed several cross-correlation analyses. They found that the TeV and X-ray light curves were very well correlated, with a lag of less than 0.6 days. The GeV and 15 GHz radio light curves also showed correlation, with a lag of over 30-100 days. However, no correlation was observed between the TeV and the radio light curves. They suggested that the variability at high energy may be due to the leptonic mechanism, given the short time scale of variability.

Although extensive multiwavelength studies on Mrk 421 have been extensively conducted to date, research on its radio spectrum has been limited. In particular, simultaneous multifrequency very long baseline interferometry (VLBI) imaging observations with high time resolution have not been performed yet. In this study, we present various analyses of the radio spectrum of Mrk 421 to explain the correlation between the spectrum and the flux density variations.

In this paper, we report results from simultaneous multifrequency VLBI observations of Mrk 421 carried out using the Korea VLBI Network (KVN) at 22, 43, and 86, from January 2013 to June 2018. The paper is organized as follows. In Section 2, we present descriptions of the observations for both the KVN and all archival data used in this paper. Section 3 and 4 describe the results and various analyses of flux density variability at multiple frequencies, respectively. Finally, Section 5 includes a discussion on the results and analysis.

2. OBSERVATIONS AND DATA CALIBRATION

2.1. KVN observations

We conducted simultaneous multifrequency VLBI imaging monitoring observations of Mrk 421 using the Korean VLBI Network (KVN) at 22, 43, 86, and 129 GHz as part of the iMOGABA (Interferometric Monitoring of Gamma-ray Bright active galactic Nuclei) project (Lee et al. 2016, 2017b; Algaba et al. 2018; Lee et al. 2020; Kang et al. 2021). The KVN is a VLBI network system consisting of three 21-meter radio telescopes located in Seoul (KVN Yonsei), Ulsan (KVN Ulsan), and Jeju (KVN Tamna), Korea. The monitoring observations were primarily carried out every month. However, we excluded the 129 GHz data from the analysis because there were no valid measurements, higher than $3\text{-}\sigma$ of errors. The observation period was from January 2013 to June 2018, except for maintenance periods from June to August. Measurements were made in 41 epochs over a period of 5.5 years. At 22, 43, and 86 GHz, 40 epochs, 33 epochs, and 21 epochs were measured, respectively. The observing frequencies were 21.700-21.764, 43.400-43.464, 86.800-86.864, and 129.300-129.364 GHz, with a total bandwidth of 256 MHz. The angular resolutions of the KVN were 6, 3, and 1.5 mas at 22, 43, and 86 GHz, respectively. We used a left circular polarization observation mode at a recording rate of 1 Gbps. For more details of the KVN observations, see Lee et al. (2016, 2017a).

2.2. Data calibration

The observed data were processed using the DiFX software correlator in Daejeon, Korea (Deller et al. 2007; Lee et al. 2015). The DiFX correlator generated a cross-correlation function spectrum with a resolution of 0.125 MHz and an accumulation period of one second. After the correlation, the data was calibrated with the AIPS (Astronomy Image Processing System) software package, provided by the National Radio Astronomy Observatory (NRAO), following standard procedures, including phase and amplitude calibration, fringe fitting, and bandpass calibration. We used the KVN pipeline developed by Hodgson et al. (2016) to perform the data calibration. Sensitivity at high frequencies was improved by transferring phase solutions from lower to higher frequencies (i.e., FPT) as described by Rioja & Dodson (2011) and Algaba et al. (2015). Amplitude calibration was conducted using the system temperatures measured during the observations. The system temperatures were adjusted for atmospheric opacity based on sky-tipping curve measurements conducted every hour at each radio telescope. Renormalization of the fringe amplitudes was conducted to correct the amplitude distortion due to quantization, and losses from quantization and re-quantization were corrected

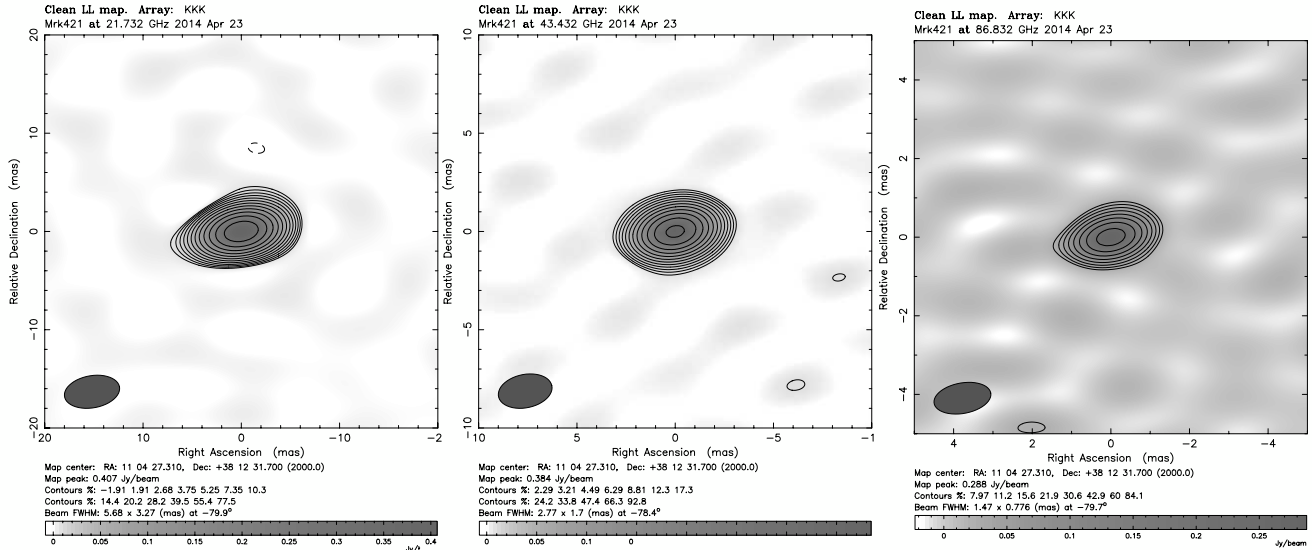


Figure 1. CLEAN maps of Mrk 421 obtained in Epoch 14 (April 23, 2014). The left, middle, and right panels indicate source structures at 22, 43, and 86 GHz, respectively. The source shows a compact core-dominated structure at all frequencies. The contour level starts from 3 times the noise and increases by a factor of $\sqrt{2}$. The beam size is indicated by the filled ellipse in the bottom left corner.

(Lee et al. 2015). After the amplitude calibration and the re-quantization loss calibration, the uncertainty of the amplitude calibration was within 5% at 22 and 43 GHz and 10-30% at 86 and 129 GHz.

2.3. Imaging and modelfitting

After the phase and amplitude calibration, we used DIFMAP to make a CLEAN contour map. To make a CLEAN map with the phase self-calibration, for the first time we performed the startmod command. This uses a point source model of 1 Jy to conduct the initial phase self-calibration. Then, the visibility data at 22, 43, and 86 GHz were averaged at 30-second intervals. This averaging time aligned with the typical coherence timescales of KVN observations. We flagged bad amplitude and phase data points and outliers in the vplot. Then, the repetitive CLEANing and phase self-calibration within the central emitting regions were performed until the noise root-mean-square (rms) level was no longer significantly lowered. The standard CLEANing and self-calibration within the central emitting regions were conducted until no significant flux density was added compared to the image rms level.

Since Mrk 421 is a compact source observed on mas-scales in the KVN observations, finding the best model is straightforward. Figure 1 displays the CLEAN contour maps of Mrk 421 at 22, 43, and 86 GHz for a representative epoch (well observed at all frequencies) showing compact core-dominated components. After making the CLEAN contour map, we computed the image quality factor ξ_r . This is the ratio of the image rms noise and its mathematical expectation, $\xi_r = S_r/S_{r,\text{exp}}$, where S_r is the maximum absolute flux density in the residual image, and $S_{r,\text{exp}}$ is the expectation of S_r . For a more comprehensive understanding of this image quality evaluation scheme, please refer

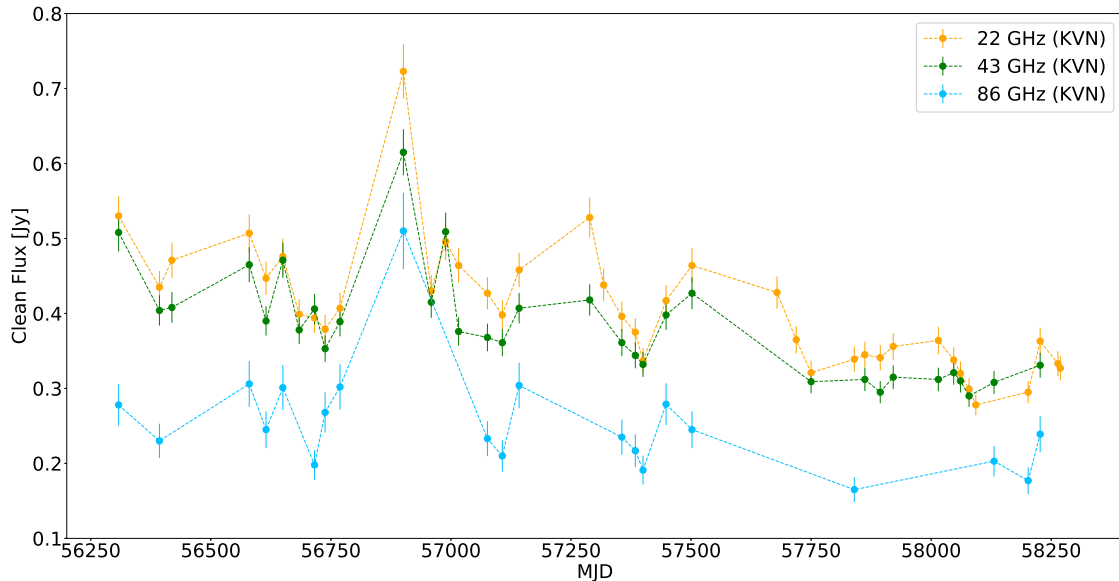


Figure 2. Light curves of Mrk 421. Yellow, green, and sky blue dots indicate 22, 43, and 86 GHz, respectively.

to Lobanov et al. (2006) and Lee et al. (2016, 2017a). The ξ_r values derived in this paper range from 0.65 - 0.97, suggesting that the images sufficiently represent the structure identified in the visibility data.

To establish the model of the source, we fit the model in the uv -data. In this process, we used a single circular two-dimensional Gaussian model to obtain the model parameters, the information of the model, such as flux, size, and degree of the major axis. The model fitting was repeated until reduced χ^2 approached one, and model fitting stops when the reduced χ^2 does not decrease anymore.

Table 1 lists the fitted parameters, including the observing frequencies, restoring beam size $B_{\text{maj,min}}$, position angle B_{PA} , total CLEAN flux density S_{KVN} , peak flux density S_p in units of Jy per beam, rms in the image σ , the dynamic range (ratio of peak to rms) of the image D, and image quality factor ξ_r .

3. RESULTS

3.1. Multifrequency light curves

We present the results of the multifrequency radio observations of Mrk 421. Figure 2 displays the multifrequency light curves of Mrk 421 at 22, 43, and 86 GHz observed between January 16, 2013 (MJD 56308) and June 1, 2018 (MJD 58270). During the 5.5-year observation period, the flux density gradually decreases and several small flux enhancements are shown (which we call flares). The light curves show a similar trend at all frequencies. Although we can't show the 15 GHz light curve of the OVRO in this study, the 15 GHz light curve exhibits flux enhancements peaking at approximately MJD 56400, 56900, and 57200 (see Figure 1 in Arbet-Engels et al. 2021). In the KVN light curves, only the flare at MJD 56900 is seen due to the relatively sparse data points. Because of that, the flare at MJD 56900 looks like a large flare. But the flare is very sharp indeed.

Table 1. Image parameters

Epoch	MJD	Band	B_{maj}	B_{min}	B_{PA}	S_{KVN}	S_{p}	σ	D	ξ_{r}
			(mas)	(mas)	($^{\circ}$)	(Jy)	(Jy/beam)	(mJy/beam)		
(1)	(2)	(3)	(4)	(5)	(6)	(7)	(8)	(9)	(10)	(11)
2013 Jan 16	56308	K	0.300	0.189	-89.9	0.530	0.523	3	193	0.73
2013 Jan 16	56308	Q	0.148	0.094	-85.2	0.508	0.496	6	89	0.72
2013 Jan 16	56308	W	0.077	0.045	-72.6	0.278	0.281	11	26	0.75
2013 Apr 11	56393	K	0.299	0.182	-82.7	0.435	0.435	4	103	0.79
2013 Apr 11	56393	Q	0.147	0.096	-78.7	0.404	0.401	7	55	0.72
2013 Apr 11	56393	W	0.076	0.043	-83.1	0.230	0.218	16	13	0.70
2013 May 07	56419	K	0.300	0.180	-77.9	0.471	0.470	5	87	0.75
2013 May 07	56419	Q	0.149	0.093	-77.2	0.408	0.404	11	35	0.68
2013 Oct 15	56580	K	0.303	0.176	-77.2	0.507	0.505	5	95	0.82
2013 Oct 15	56580	Q	0.151	0.089	-77.5	0.465	0.436	10	42	0.76
2013 Oct 15	56580	W	0.077	0.043	-85.8	0.306	0.217	26	8	0.78
2013 Nov 19	56615	K	0.304	0.179	-81.0	0.447	0.446	3	144	0.72
2013 Nov 19	56615	Q	0.153	0.086	-84.2	0.390	0.369	5	79	0.80
2013 Nov 19	56615	W	0.078	0.043	87.3	0.245	0.208	8	26	0.73
2013 Dec 24	56650	K	0.283	0.170	79.6	0.476	0.472	6	84	0.74
2013 Dec 24	56650	Q	0.146	0.086	79.5	0.471	0.446	7	65	0.83
2013 Dec 24	56650	W	0.070	0.042	82.9	0.301	0.285	9	33	0.82
2014 Jan 27	56684	K	0.298	0.187	-83.5	0.399	0.398	4	113	0.74
2014 Jan 27	56684	Q	0.148	0.098	-79.6	0.378	0.368	5	75	0.71
2014 Feb 28	56716	K	0.376	0.164	-63.9	0.394	0.393	5	76	0.72
2014 Feb 28	56716	Q	0.176	0.086	-63.6	0.406	0.400	9	47	0.81
2014 Feb 28	56716	W	0.113	0.037	-62.1	0.198	0.216	11	20	0.74
2014 Mar 22	56738	K	0.309	0.172	-85.6	0.379	0.379	4	108	0.73
2014 Mar 22	56738	Q	0.150	0.091	-85.7	0.353	0.353	6	61	0.83
2014 Mar 22	56738	W	0.082	0.041	89.8	0.268	0.253	10	26	0.80
2014 Apr 22	56769	K	0.304	0.175	-79.9	0.407	0.407	2	171	0.83
2014 Apr 22	56769	Q	0.148	0.091	-78.4	0.389	0.384	3	131	0.79
2014 Apr 22	56769	W	0.078	0.042	-79.7	0.302	0.286	8	37	0.85
2014 Sep 01	56901	K	0.300	0.180	-80.1	0.723	0.720	7	99	0.83
2014 Sep 01	56901	Q	0.142	0.095	-82.1	0.615	0.616	6	110	0.70
2014 Sep 01	56901	W	0.078	0.043	-76.9	0.510	0.481	27	18	0.92
2014 Oct 29	56959	K	0.330	0.160	86.2	0.430	0.428	5	79	0.74
2014 Oct 29	56959	Q	0.174	0.075	-84.3	0.415	0.404	7	56	0.79
2014 Nov 28	56989	K	0.334	0.164	-76.9	0.496	0.492	8	64	0.83
2014 Nov 28	56989	Q	0.169	0.084	-70.2	0.509	0.508	9	57	0.70
2014 Dec 25	57016	K	0.324	0.162	-84.6	0.464	0.462	6	78	0.87
2014 Dec 25	57016	Q	0.148	0.090	-82.8	0.376	0.384	10	37	0.89
2015 Feb 23	57076	K	0.312	0.170	-80.3	0.427	0.425	4	109	0.93

Table 1 continued on next page

Table 1 (*continued*)

Epoch	MJD	Band	B_{maj}	B_{min}	B_{PA}	S_{KVN}	S_{p}	σ	D	ξ_{r}
			(mas)	(mas)	($^{\circ}$)	(Jy)	(Jy/beam)	(mJy/beam)		
(1)	(2)	(3)	(4)	(5)	(6)	(7)	(8)	(9)	(10)	(11)
2015 Feb 23	57076	Q	0.149	0.094	-78.8	0.368	0.365	3	115	0.77
2015 Feb 23	57076	W	0.078	0.042	-77.7	0.233	0.220	7	34	0.84
2015 Mar 26	57107	K	0.312	0.168	-84.2	0.398	0.396	4	111	0.98
2015 Mar 26	57107	Q	0.147	0.091	-81.9	0.361	0.353	2	144	0.80
2015 Mar 26	57107	W	0.079	0.041	-83.6	0.210	0.191	6	34	0.78
2015 Apr 30	57142	K	0.323	0.163	-77.8	0.458	0.456	7	69	0.85
2015 Apr 30	57142	Q	0.149	0.088	-81.9	0.407	0.404	4	110	0.84
2015 Apr 30	57142	W	0.082	0.040	-78.0	0.304	0.288	11	25	0.79
2015 Sep 24	57289	K	0.316	0.171	-69.6	0.528	0.528	6	95	0.84
2015 Sep 24	57289	Q	0.156	0.083	-77.2	0.418	0.420	10	43	0.74
2015 Oct 23	57318	K	0.347	0.165	80.8	0.438	0.436	9	46	0.81
2015 Nov 30	57356	K	0.293	0.181	-86.9	0.396	0.396	4	96	0.89
2015 Nov 30	57356	Q	0.141	0.096	-87.0	0.361	0.363	4	83	0.78
2015 Nov 30	57356	W	0.076	0.043	-86.2	0.235	0.218	8	27	0.85
2015 Dec 28	57384	K	0.300	0.175	-85.1	0.375	0.375	3	125	0.83
2015 Dec 28	57384	Q	0.147	0.091	-81.1	0.344	0.343	2	144	0.78
2015 Dec 28	57384	W	0.080	0.041	-85.3	0.217	0.202	6	36	0.79
2016 Jan 13	57400	K	0.303	0.174	-88.6	0.337	0.337	2	139	0.71
2016 Jan 13	57400	Q	0.147	0.091	-84.3	0.332	0.321	2	135	0.79
2016 Jan 13	57400	W	0.080	0.041	89.5	0.191	0.164	6	26	0.84
2016 Mar 01	57448	K	0.303	0.173	-85.4	0.417	0.417	3	123	0.90
2016 Mar 01	57448	Q	0.149	0.089	-85.1	0.398	0.392	3	119	0.81
2016 Mar 01	57448	W	0.077	0.042	-86.5	0.279	0.259	9	29	0.81
2016 Apr 24	57502	K	0.301	0.185	-81.8	0.464	0.465	5	88	0.94
2016 Apr 24	57502	Q	0.152	0.091	-80.9	0.427	0.410	3	117	0.90
2016 Apr 24	57502	W	0.078	0.044	-83.8	0.245	0.251	6	44	0.77
2016 Oct 18	57679	K	0.330	0.168	80.8	0.428	0.428	5	87	0.71
2016 Nov 27	57719	K	0.310	0.183	-88.6	0.365	0.365	4	86	0.89
2016 Dec 28	57750	K	0.290	0.184	-87.4	0.321	0.321	3	95	0.84
2016 Dec 28	57750	Q	0.148	0.088	89.6	0.309	0.304	4	76	0.85
2017 Mar 28	57840	K	0.372	0.172	-62.2	0.339	0.340	2	181	0.65
2017 Mar 28	57840	W	0.097	0.042	-61.7	0.165	0.149	4	37	0.85
2017 Apr 19	57862	K	0.310	0.170	-86.0	0.345	0.344	5	65	0.82
2017 Apr 19	57862	Q	0.166	0.082	84.9	0.312	0.290	8	35	0.80
2017 May 21	57894	K	0.316	0.174	83.9	0.341	0.341	5	68	0.78
2017 May 21	57894	Q	0.168	0.081	80.3	0.295	0.282	4	68	0.75
2017 Jun 17	57921	K	0.310	0.174	-77.3	0.356	0.355	5	75	0.93
2017 Jun 17	57921	Q	0.164	0.080	-80.2	0.315	0.302	3	101	0.78
2017 Sep 19	58015	K	0.321	0.180	-78.4	0.364	0.365	7	53	0.83

Table 1 continued on next page

Table 1 (continued)

Epoch	MJD	Band	B_{maj}	B_{min}	B_{PA}	S_{KVN}	S_{p}	σ	D	ξ_{r}
			(mas)	(mas)	($^{\circ}$)	(Jy)	(Jy/beam)	(mJy/beam)		
(1)	(2)	(3)	(4)	(5)	(6)	(7)	(8)	(9)	(10)	(11)
2017 Sep 19	58015	Q	0.165	0.083	-78.9	0.312	0.308	3	98	0.80
2017 Oct 21	58047	K	0.307	0.176	85.4	0.338	0.338	3	133	0.86
2017 Oct 21	58047	Q	0.162	0.084	79.7	0.321	0.310	3	120	0.80
2017 Nov 04	58061	K	0.330	0.185	-68.5	0.320	0.320	4	87	0.87
2017 Nov 04	58061	Q	0.178	0.086	-69.0	0.310	0.301	4	79	0.77
2017 Nov 22	58079	K	0.293	0.183	-84.4	0.299	0.298	4	82	0.85
2017 Nov 22	58079	Q	0.156	0.085	-89.1	0.290	0.281	4	80	1.00
2017 Dec 06	58093	K	0.296	0.178	-88.3	0.278	0.275	5	51	0.97
2018 Jan 13	58131	Q	0.158	0.084	88.2	0.308	0.302	2	159	0.77
2018 Jan 13	58131	W	0.075	0.043	-85.3	0.203	0.189	6	31	0.78
2018 Mar 25	58202	K	0.300	0.184	-79.8	0.295	0.290	11	27	0.82
2018 Mar 25	58202	W	0.085	0.042	-73.3	0.177	0.224	32	7	0.71
2018 Apr 19	58227	K	0.307	0.174	-88.7	0.363	0.362	6	60	0.89
2018 Apr 19	58227	Q	0.157	0.083	89.6	0.331	0.321	3	95	0.84
2018 Apr 19	58227	W	0.082	0.040	88.8	0.239	0.244	11	22	0.95
2018 May 26	58264	K	0.303	0.181	83.9	0.333	0.333	7	47	0.84
2018 May 31	58269	K	0.331	0.171	80.0	0.327	0.327	8	41	0.79

NOTE— Column designation: 1 - Date; 2 - modified Julian date; 3 - observing frequency band: K - 22 GHz band; Q - 43 GHz band; W - 86 GHz band; D - 129 GHz band; 4-6 - restoring beam: 4 - major axis; 5 - minor axis; 6 - position angle of the major axis; 7 - total CLEAN KVN flux density; 8 - peak flux density; 9 - off-source RMS in the image; 10 - dynamic range of the image; 11 - quality of the residual noise in the image (i.e., the ratio of the image root-mean-square noise to its mathematical expectation).

4. ANALYSIS

4.1. Radio spectrum

The simultaneous multifrequency monitoring KVN observations enable us to investigate source spectra accurately without the time uncertainty. The multifrequency spectral analyses of variable blazars using arcsecond-scale observations by Kim et al. (2022) and Jeong et al. (2023) show that variable spectral properties can be revealed by subtracting off the quiescent spectrum in the multifrequency light curves. We calculated the quiescent spectrum by fitting the four local minima obtained on MJD 56716, 57107, 57400, and 57840 - 58093 shown in Figure 3. The fourth local minimum we used is obtained on MJD 58093 at 22 GHz, MJD 58079 at 43 GHz, and MJD 57840 at 86 GHz. The quiescent spectrum is obtained as 0.263 ± 0.045 Jy, 0.271 ± 0.021 Jy, and 0.156 ± 0.027 Jy at 22, 43, and 86 GHz, respectively, by extrapolating each of the three frequencies to a common time (MJD 58269), as shown in Figure 4.

The mas-scale spectra of Mrk 421 are shown in Figure 5. Out of the 41 epochs, data existed for at least two frequencies for 33 epochs. The observed spectrum is shown in black, and the quiescent-corrected spectrum (the observed spectrum by subtracting the quiescent spectrum) is shown in red. The spectra generally appear to be flat between 22 and 43 GHz, and seem to be relatively steep between 43 and 86 GHz. The quiescent-corrected spectra are sometimes consistent with the observed spectra and sometimes quite different. Unlike the observed spectra, the quiescent-corrected spectra generally show inverted spectra between 22 and 43 GHz. Although we were not able to precisely calculate the turnover frequency, ν_c , of Mrk 421 in this analysis, we clearly find that the quiescent-corrected spectrum becomes steeper between 22 and 43 GHz and flatter between 43 and 86 GHz than the observed spectrum. This implies that the quiescent emission correction for the source spectrum in the mas-scale may be important to study the intrinsic spectral properties of the variable emission regions.

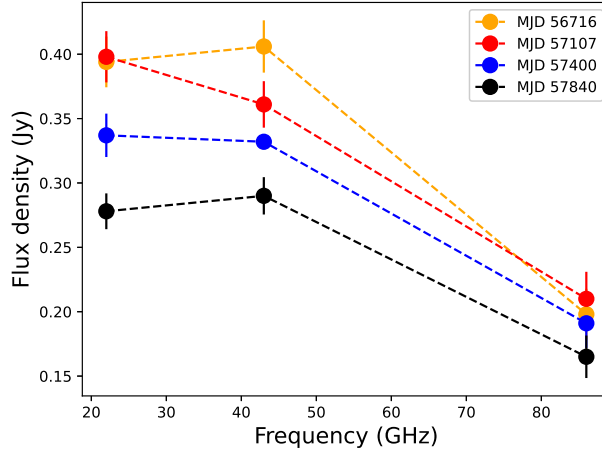


Figure 3. Plot of local minima on MJD 56716, 57107, 57400, and 57840 - 58093.

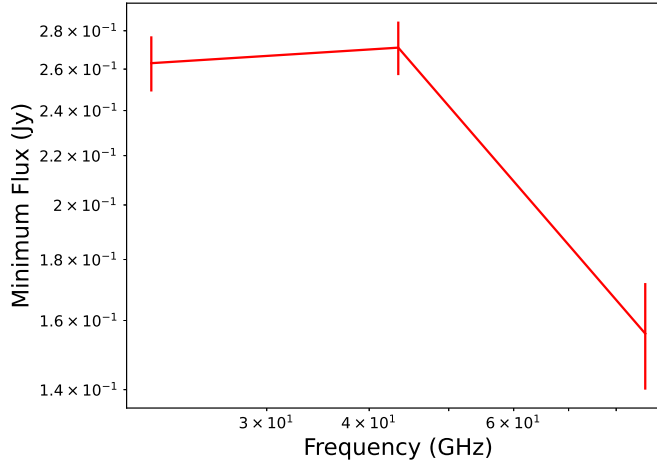


Figure 4. The minimum flux density at each frequency, by fitting the four local minima obtained on MJD 56716, 57107, 57400, and 57840 - 58093, and extrapolating each of the three frequencies to a common time (MJD 58269).

4.2. Spectral index

The spectral index α is defined as $S_\nu \propto \nu^\alpha$, where ν is the observing frequency, and S_ν is the flux density. We calculated α for the data pairs 22 and 43 GHz, $\alpha_{22/43}$, and 43 and 86 GHz, $\alpha_{43/86}$ (see Figure 6). The range of observed $\alpha_{22/43}$ was $-0.34 - 0.04$ with a mean $\alpha_{22/43}$ of -0.12 , and $\alpha_{43/86}$ was $-1.04 - -0.27$ with a mean $\alpha_{43/86}$ of -0.63 . The $\alpha_{22/43}$ was relatively flat, and $\alpha_{43/86}$ was steep. As before, we calculated the quiescent-corrected spectral indices. The range of the quiescent-corrected spectral indices between 22 and 43 GHz $\alpha_{cor,22/43}$ was $-1.7 - 0.04$ with a mean $\alpha_{cor,22/43}$ of -0.57 . For 43 and 86 GHz, the range of the quiescent-corrected spectral indices $\alpha_{cor,43/86}$ was $-1.69 - -0.47$ with a mean $\alpha_{cor,43/86}$ of -0.33 .

In Figure 6, we see that the 22 and 43 GHz quiescent-corrected spectral indices are consistently lower (steeper) than the observed spectral indices, although the errors are large. We noticed that the values of $\alpha_{22/43}$ were steeper when the flares were around the peaks on MJD 56901 and MJD 57289, whereas those were flatter at local minima (MJD 56716 and MJD 57400).

The 43 and 86 GHz quiescent-corrected spectral indices showed more variability with spectral indices that were sometimes consistent, sometimes lower, and sometimes higher than the observed spectral indices, although the errors were large. To further investigate the effect of correcting for the quiescent spectrum, we plotted the spectral indices versus flux density. In Figures 7 - 8, a) and b) indicate the observed spectral index, and c) and d) indicate the

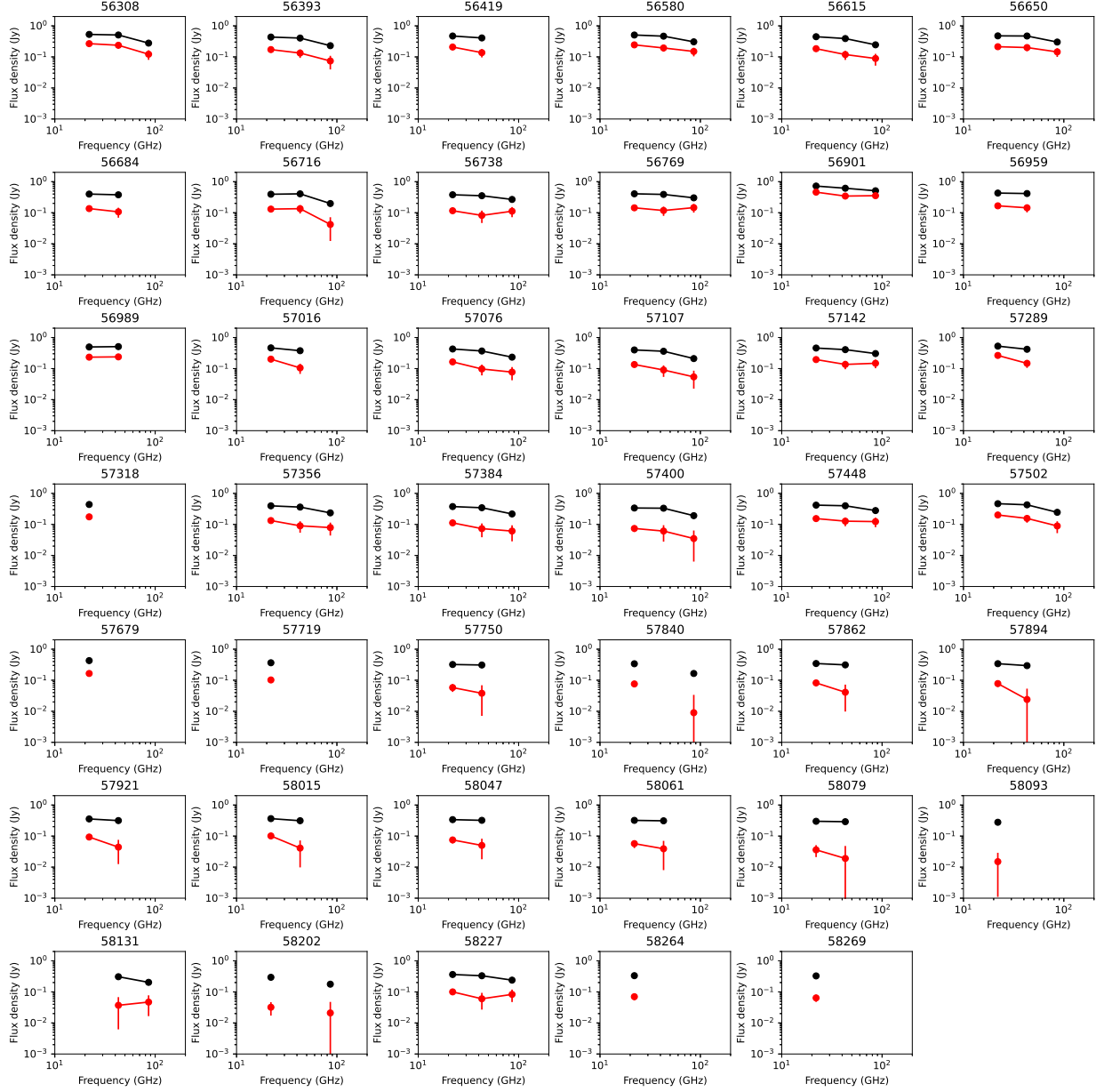


Figure 5. Spectrum of Mrk 421. Black and red symbols represent the observed spectrum and quiescent-corrected spectrum, respectively.

quiescent-corrected spectral index versus flux density, respectively. To analyze the relation between the spectral index and flux density quantitatively, we computed the Spearman correlation coefficient ρ and probability p for each case. The values of ρ of $\alpha_{22/43}$ for 22 GHz and 43 GHz flux density were -0.24 and 0.04 , respectively. The values of ρ of $\alpha_{cor,22/43}$ for 22 GHz and for 43 GHz flux density were 0.4 and 0.66 , respectively. The values of ρ of $\alpha_{43/86}$ for 43 GHz and for 86 GHz were -0.11 and 0.6 , respectively. The values of ρ of $\alpha_{cor,43/86}$ for 43 GHz and for 86 GHz were -0.44 and 0.33 , respectively.

The original 22 and 43 GHz spectral indices were uncorrelated with the flux densities. For the quiescent-corrected spectral indices (c and d), the spectral indices and flux densities showed a significant correlation (See, Figure 7). In Figure 8, there is no correlation between $\alpha_{43/86}$ and the 43 GHz flux density, but the $\alpha_{43/86}$ is correlated with 86 GHz flux density. The $\alpha_{43/86}$ increases with the 86 GHz flux density. In the quiescent-corrected case, we now see an anti-correlation between the corrected spectral indices vs. 43 GHz flux densities. The quiescent-corrected spectral

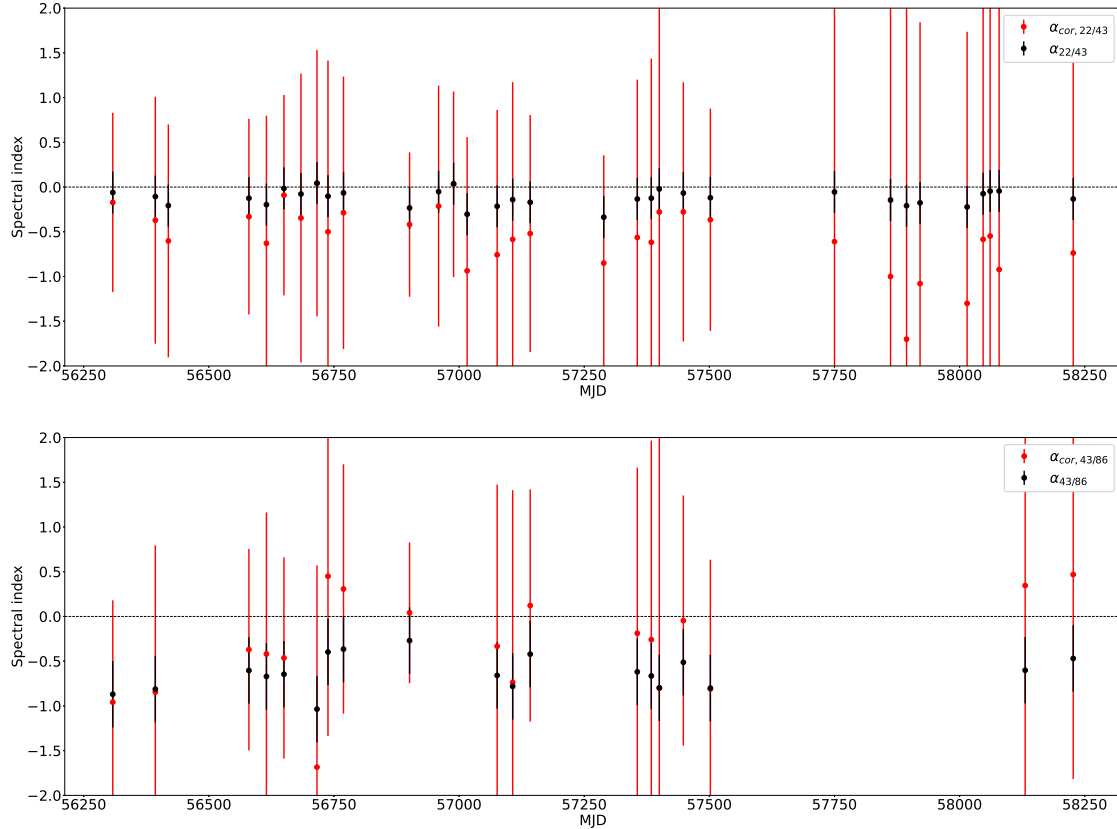


Figure 6. Spectral index α of Mrk 421. The top panel is $\alpha_{22/43}$ and the bottom panel is $\alpha_{43/86}$. The red symbols indicate the quiescent-corrected spectral index. A horizontal line is a guideline of zero.

indices were less correlated with the 86 GHz flux densities than before.

5. DISCUSSION

Figures 7 and 8 show that correcting for the quiescent spectrum can significantly affect the measurements of the spectral indices. This is of particular importance for calculations that require measurements of the synchrotron self-absorption frequency, for example, the magnetic field strength, $B_{\text{SSA}} \propto \nu_c^5$. This means that even small errors in measuring ν_c can lead to significant errors when measuring the magnetic field strength. This suggests that magnetic field strength estimations based on multifrequency data should be carefully obtained with a proper determination of the optically thin quiescent spectrum of compact radio sources even on mas-scales.

To test the previous work, which did not consider correcting the quiescent spectrum, we re-analyzed the multifrequency spectral properties of OJ 287 (Lee et al. 2020). The minimum flux densities of OJ 287 were 2.58, 2.27, 1.83, and 1.36 at 22, 43, 86, and 129 GHz, respectively. The spectral index between 86 and 129 GHz was -0.73 . We used this optically thin spectral index to correct the observed spectrum. We subtracted the minimum flux density obtained from the optically thin spectral index at each frequency for 8 epochs analyzed in Lee et al. (2020). Figure 9 shows the spectra of OJ 287. The black and grey symbols indicate the observed and the quiescent-corrected spectra, respectively. After subtracting the optically thin spectrum, the spectrum was fitted with a curved power-law function (Lee et al. 2016, 2017b, 2020). Then, we obtained the turnover frequency and the peak flux density. The turnover frequencies ob-

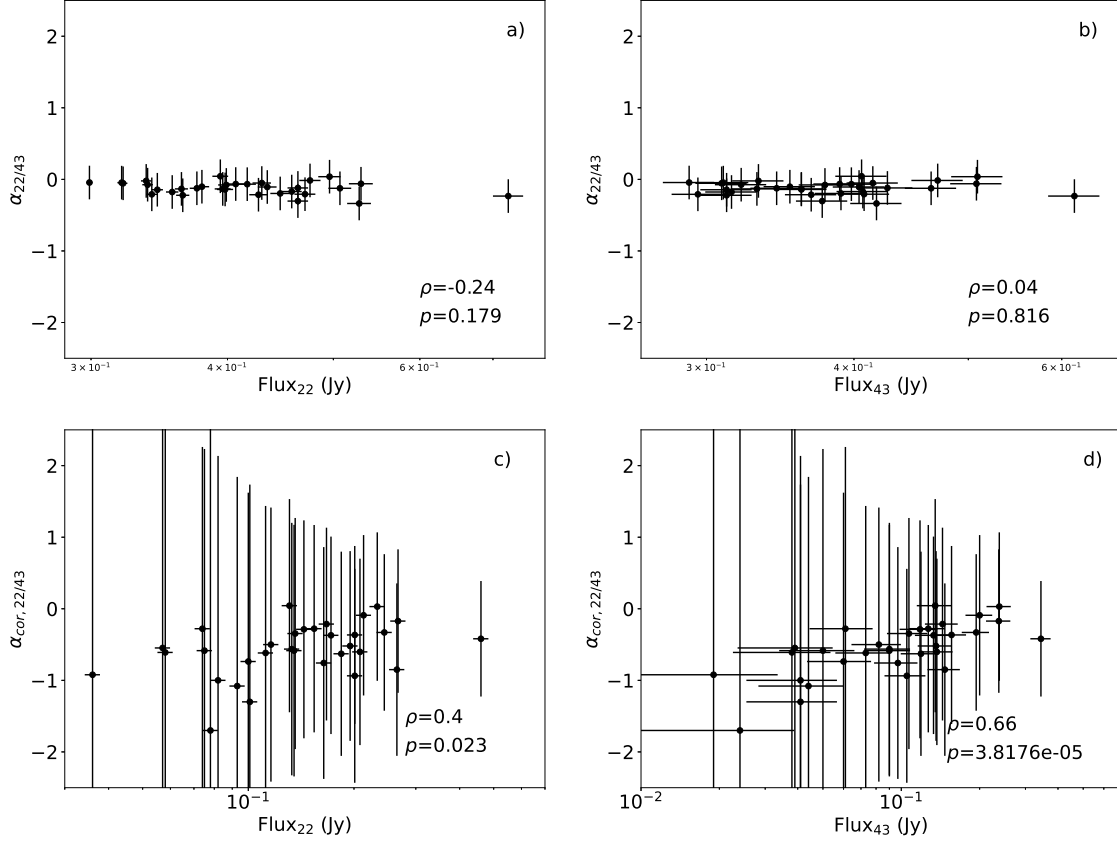


Figure 7. Spectral index as a function of the flux density. The left and right panels indicate 22 and 43 GHz, respectively. a) and b) indicate α vs. flux density. c) and d) indicate the α_{cor} vs. flux density. ρ and p values indicate coefficient and probability, respectively.

tained from the quiescent-corrected spectra were in the range of 28-80 GHz, and the peak flux densities were 0.7-3.3 Jy. The turnover frequencies were larger by a factor of approximately 2.5 larger than the ones obtained from the observed spectra. Because of the $B_{SSA} \propto \nu_c^5$, the synchrotron self-absorption magnetic field strength might be underestimated in Lee et al. (2020). This could also potentially change the comparison result between the equipartition magnetic field strength and synchrotron self-absorption magnetic field strength.

6. SUMMARY

We have presented the results of simultaneous multifrequency observations at 22, 43, and 86 GHz with the KVN. The light curves showed a global decaying and several small radio flares. To separate the variable component and the quiescent component in the light curves, we subtracted the quiescent component, assuming the minimum flux density. We found that the observed spectra were flat at 22-43 GHz, and relatively steep at 43-86 GHz, whereas the quiescent-corrected spectra are sometimes quite different from the observed spectra (e.g., sometimes inverted at 22-43 GHz). This means that the turnover frequency, ν_c is shifted to a higher frequency. Based on the assumption of the synchrotron self-absorption magnetic field strength estimation, $B_{SSA} \propto \nu_c^5$. Therefore, to properly estimate the magnetic field strength, subtracting the quiescent spectrum in the KVN light curves is important.

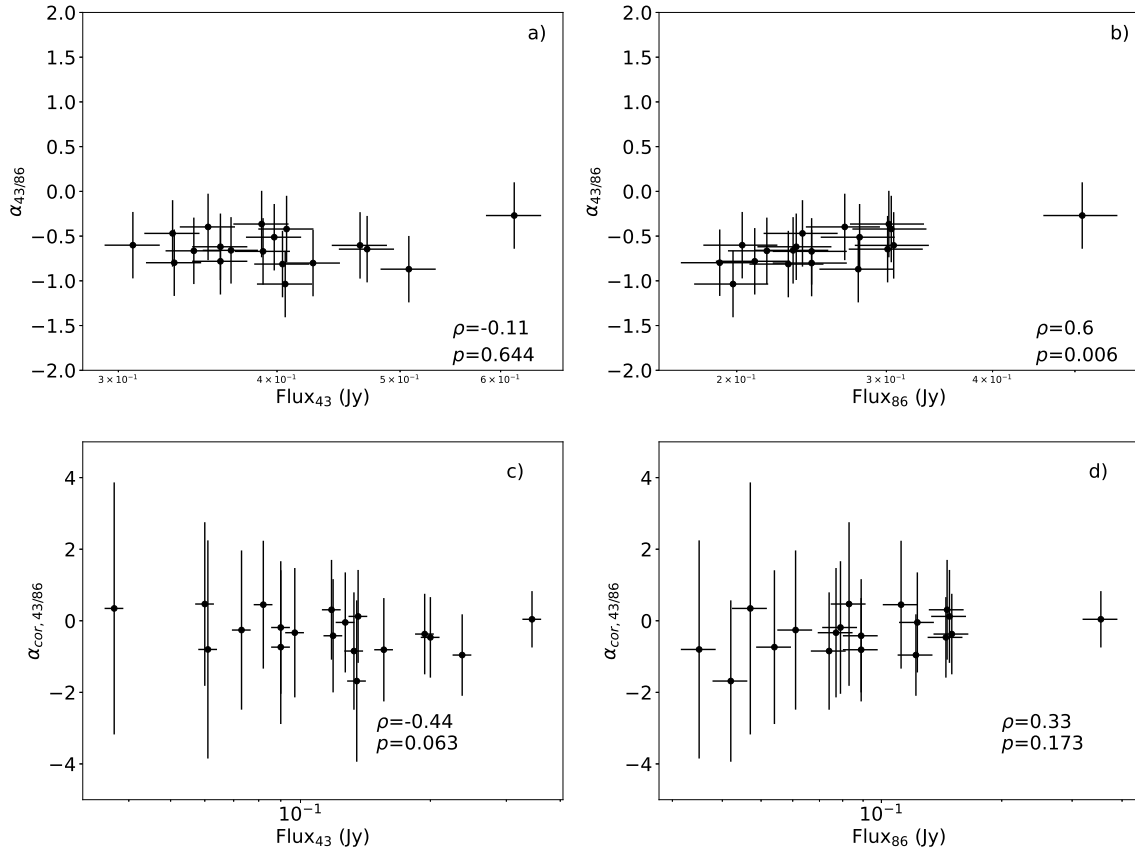


Figure 8. Spectral index as a function of the flux density. The left and right panels indicate 43 and 86 GHz, respectively. a) and b) indicate α vs. flux density. c) and d) indicate the α_{cor} vs. flux density. ρ and p values indicate coefficient and probability, respectively.

We thank the anonymous reviewer for valuable comments and suggestions that helped to improve the paper. We are grateful to all staff members in KVN who helped to operate the array and to correlate the data. The KVN is a facility operated by the Korea Astronomy and Space Science Institute. The KVN operations are supported by KREONET (Korea Research Environment Open NETwork) which is managed and operated by KISTI (Korea Institute of Science and Technology Information). This work was supported by the National Research Foundation of Korea (NRF) grant funded by the Korea government (MIST) (2020R1A2C2009003).

REFERENCES

- Acciari, V. A., Aliu, E., Arlen, T., et al. 2011, ApJ, 738, 25. doi:10.1088/0004-637X/738/1/25
- Aleksić, J., Ansoldi, S., Antonelli, L. A., et al. 2015, A&A, 576, A126. doi:10.1051/0004-6361/201424216
- Algaba, J.-C., Zhao, G.-Y., Lee, S.-S., et al. 2015, Journal of Korean Astronomical Society, 48, 237. doi:10.5303/JKAS.2015.48.5.237
- Algaba, J.-C., Lee, S.-S., Kim, D.-W., et al. 2018, ApJ, 852, 30. doi:10.3847/1538-4357/aa9e50
- Arbet-Engels, A., Baack, D., Balbo, M., et al. 2021, A&A, 647, A88. doi:10.1051/0004-6361/201935557
- Charlot, P., Gabuzda, D. C., Sol, H., et al. 2006, A&A, 457, 455. doi:10.1051/0004-6361:20054078
- Deller, A. T., Tingay, S. J., Bailes, M., et al. 2007, PASP, 119, 318. doi:10.1086/513572

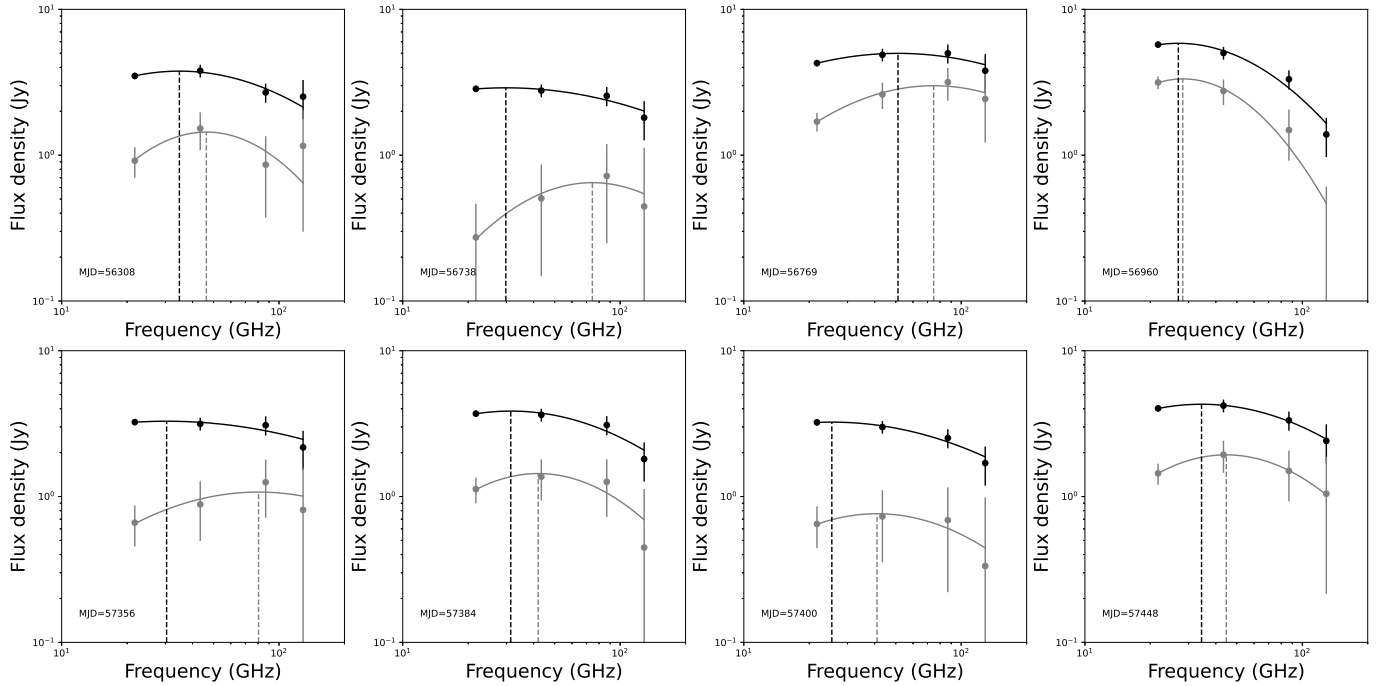


Figure 9. The spectra of OJ 287. Black and grey symbols indicate the original and the quiescent-corrected spectra, respectively. Black and grey vertical lines correspond to the turnover frequency at the original spectrum and the quiescent-corrected spectrum, respectively.

Hodgson, J., Lee, S.-S., Zhao, G.-Y., et al. 2016, JKAS, 49, 137

Horan, D., Acciari, V. A., Bradbury, S. M., et al. 2009, ApJ, 695, 596. doi:10.1088/0004-637X/695/1/596

Jeong, H.-W., Lee, S.-S., Cheong, W. Y., et al. 2023, MNRAS, 523, 5703. doi:10.1093/mnras/stad1736

Kang, S., Lee, S.-S., Hodgson, J., et al. 2021, A&A, 651, A74. doi:10.1051/0004-6361/202040198

Katarzyński, K., Sol, H., & Kus, A. 2003, A&A, 410, 101. doi:10.1051/0004-6361:20031245

Kim, S.-H., Lee, S.-S., Lee, J. W., et al. 2022, MNRAS, 510, 815. doi:10.1093/mnras/stab3473

Lee, S.-S., Byun, D.-Y., Oh, C. S., et al. 2015, Journal of Korean Astronomical Society, 48, 229. doi:10.5303/JKAS.2015.48.5.229

Lee, S.-S., Wajima, K., Algaba, J.-C., et al. 2016, ApJS, 227, 8

Lee, J. W., Lee, S.-S., Hodgson, J. A., et al. 2017a, ApJ, 841, 119

Lee, J. W., Sohn, B. W., Byun, D.-Y., Lee, J. A., & Kim, S. S. 2017b, A&A, 601, A12

Lee, J. W., Lee, S.-S., Algaba, J.-C., et al. 2020, ApJ, 902, 104. doi:10.3847/1538-4357/abb4e5

Lobanov, A. P., Krichbaum, T. P., Witzel, A., et al. 2006, PASJ, 58, 253. doi:10.1093/pasj/58.2.253

Punch, M., Akerlof, C. W., Cawley, M. F., et al. 1992, Nature, 358, 477. doi:10.1038/358477a0

Rioja, M. & Dodson, R. 2011, AJ, 141, 114. doi:10.1088/0004-6256/141/4/114

Ulrich, M.-H., Maraschi, L., & Urry, C. M. 1997, ARA&A, 35, 445. doi:10.1146/annurev.astro.35.1.445

Urry, C. M. & Padovani, P. 1995, PASP, 107, 803. doi:10.1086/133630

Zhu, Q., Yan, D., Zhang, P., et al. 2016, MNRAS, 463, 4481. doi:10.1093/mnras/stw2346